Biomaterials Advances 153 (2023) 213557

Contents lists available at ScienceDirect

Biomaterials Advances

journal homepage: www.journals.elsevier.com/materials-science-and-engineering-c

Combining microfluidics and coaxial 3D-bioprinting for the manufacturing of diabetic wound healing dressings

Costanza Fratini [a,b], Edward Weaver [a], Sofia Moroni [a,b], Robyn Irwin [a], Yahya H. Dallal Bashi [a], Shahid Uddin [c], Luca Casettari [b], Matthew P. Wylie [a], Dimitrios A. Lamprou [a,*]

[a] School of Pharmacy, Queen's University Belfast, 97 Lisburn Road, Belfast BT9 7BL, United Kingdom
[b] Department of Biomolecular Sciences, University of Urbino Carlo Bo, 61029 Urbino, Italy
[c] Immunocore Ltd., 92 Park Dr, Milton Park, Abingdon OX14 4RY, United Kingdom

ARTICLE INFO

Keywords:
Liposomes
Microfluidics
Hydrogels
Coaxial 3D bioprinting
Wound healing
Diabetic foot ulcers
Antibacterial scaffolds

ABSTRACT

Diabetic foot ulcers (DFUs) are a crucial complication of diabetes, as in a diabetic wound, each step of the physiological healing process is affected. This entails a more easily infectable wound, and delayed tissue regeneration due to the inflammation that occurs, leading to a drastic decrease in the overall patient's quality of life. As a strategy to manage DFUs, skin alternatives and wound dressings are currently receiving a lot of attention as they keep the wound environment "under control", while providing bioactive compounds that help to manage infection and inflammation and promote tissue repair. This has been made possible thanks to the advent of emerging technologies such as 3D Bioprinting to produce skin resembling constructs or microfluidics (MFs) that allows the manufacture of nanoparticles (NPs) that act as drug carriers, in a prompt and less expensive way.

In the present proof-of-concept study, the possibility of combining two novel and appealing techniques in the manufacturing of wound dressings has been demonstrated for first time. The novelty of this work consists in the combination of liposomes (LPs) encapsulating the active pharmaceutical ingredient (API) into a hydrogel that is further printed into a three-dimensional scaffold for wound dressing; to the knowledge of the authors this has never been done before.

A grid-shaped scaffold has been produced through the coaxial 3D bioprinting technique which has allowed to combine, in one single filament, two different bioinks. The inner core of the filament is a nanocomposite hydrogel consisting of hydroxyethyl cellulose (HEC) and PEGylated LPs encapsulated with thyme oil (TO) manufactured via MFs for the first time. The outer shell of the filament, instead, is represented by a hybrid hydrogel composed of sodium alginate/cellulose nanocrystals (SA/CNC) and enriched with free TO. This provides a combination of two different release ratios of the API, a bulk release for the first 24 h thanks to the free TO in the shell of the filament and a sustained release for up to 10 days provided from the API inside the LPs. Confocal Microscopy verified the actual presence of the LPs inside the scaffold after printing and evaluation using the zone of inhibition test proved the antibacterial activity of the manufactured scaffolds against both Gram-positive and Gram-negative bacteria.

1. Introduction

Diabetic foot ulcers (DFUs) are a worrying complication of diabetes mellitus (DM), leading to significant morbidity and mortality. According to the International Diabetes Federation, 9.1–26.1 million diabetic people will develop DFUs annually [1]. DFUs and thus the subsequent infection, are responsible for >30 % of hospitalizations and are the main cause of non-traumatic amputation [2]. Estimations worldwide have calculated that from 2.5 % to 15 % of global annual healthcare budgets are spent on DM, and medical care expense amounts to $241 billion per year [3]; therefore, DFUs don't only drastically lower the patient's quality of life, they're also an economic burden.

Even though there are well-known management strategies for DFUs, therapy is never easy. To date, a multitarget approach is the most

* Corresponding author.
E-mail address: D.Lamprou@qub.ac.uk (D.A. Lamprou).

https://doi.org/10.1016/j.bioadv.2023.213557
Received 9 May 2023; Received in revised form 21 June 2023; Accepted 7 July 2023
Available online 8 July 2023

desirable choice and consists of surgical debridement, wound dressings, off-loading, vascular assessment, treatment of active infection, and glycaemic management. Especially with the advent of novel manufacturing technologies, wound dressings that promote healing and prevent infection are of great interest. Dressings should control excessive wound exudates and maintain a moist environment in the wound, which is essential for healing processes including granulation, angiogenesis, and the migration of epidermal cells over the wound base. There are various dressing options, and several are currently being explored [1], which can be used to provide a temporary barrier against bacteria while preserving moisture in the wound region [4], and can also contain agents to combat infections and promote healing.

The biomaterials used for scaffolds targeting wound healing can be either natural or synthetic. Among the most widely used therapeutically are components isolated from extracellular matrices (ECM) such as hyaluronic acid (HA) and collagen. Polysaccharides such as chitosan (CS) and sodium alginate (SA) have also been used thanks to their intrinsic antimicrobial properties that provide an alternative to antibiotics and good ability to manage wound exudates. Besides, customizing the degradation profile of synthetic materials, can release active substances like drugs or growth factors in a regulated manner [5]. However, because most of these synthetic polymers are not bioactive, they are frequently formulated in combination with other synthetic or natural polymers to enhance their performance. The chosen scaffold needs to imitate the physiological characteristics of the skin for DFU healing to be successful [6]. It should ideally support the wound structurally while still being flexible enough to work alongside the skin's natural elasticity.

By incorporating cells, growth factors, and/or bioactive compounds including anti-inflammatory, antioxidant, and antibacterial agents, the scaffolds can also be employed as a drug delivery system (DDS). Antibiotic therapy should be targeted to aerobic Gram-positive cocci (e.g., *Staphylococcus aureus*) and Gram-negative organisms (e.g., *Pseudomonas aeruginosa, Escherichia coli*) and the DDS featuring local release may be of greater benefit [7] as due to poor angiogenesis and tissue vascularization, the local release of antibiotics and other molecules could be a more effective strategy rather than systemic administration. Moreover, systemic drug exposure can make it more likely that non-target tissues would experience toxicities and major side effects [5].

Due to increased antibiotic resistance, managing infection is increasingly difficult and it is often necessary to use new therapeutic molecules. *Thymus vulgaris,* is a native Mediterranean shrub of the *Lamiaceae* family and possesses significant antimicrobial and anti-inflammatory activity. In vivo and in vitro studies demonstrated its efficacy against antibiotic-resistant strains such as Methicillin-resistant *S. aureus* (MRSA) [8]. For these reasons, thyme oil (TO) and other essential oils (EOs) have a promising future as an all-natural antibiotic replacement [9–11]. TO has also been Generally Recognized as Safe (GRAS) by the US Food and Drug Administration (FDA) federal agency [9,12]. However, the low water solubility, chemical instability, photolability, and volatility of essential oils, limit their bioavailability [9,13]. Even so, these inconveniences may be minimized by encapsulating the EO in nanoparticulate material, a technique intended to increase shelf life, and adjust pharmacokinetics, biodistribution, and toxicological profile, while protecting the carried drug against physicochemical and enzymatic attacks [9,14,15]. One such example of nanovessels used for the encapsulation of EOs is liposomes (LPs).

Technology advancements have led to the development of novel LP manufacturing techniques, such as microfluidics (MFs), aimed at overcoming bottlenecks from previous formulation methods, such as thin film hydration, e.g., scalability and reproducibility [16,17]. MFs is a smart, high-yielding, and versatile technology; it is quick, low-cost, and dependable for creating LPs with precisely controlled characteristics and functions [18]. Its main advantage is to offer a robust and reproducible manufacturing method; therefore, reducing batch-to-batch variation. Through this technology manufacturing parameters such as chip design, flow rate ratio (FRR) or total flow rate (TFR), lipids combination and concentration [19], and mixing temperature can be easily controlled; and therefore, influence particle size, monodispersity, and encapsulation efficiency (EE) of the product obtained. Furthermore, MFs synthesis has several useful benefits, such as reduced reagent use, which is advantageous from an economical and environmentally friendly viewpoint, parallelization, and automation, which makes it perfectly suited for high-throughput optimization and scale-up [20].

Systems made up of TO encapsulated in LPs can be used for different purposes and in a variety of formulations such as solutions [21], emulsions, or nanoemulsions [14]. It has also been demonstrated that liposomal systems may be integrated into more viscous environments such as hydrogels [23,24] suggesting that there may be a further opportunity to use them to create 3D-printed scaffolds for wound healing.

3D printing (3DP), also called additive manufacturing (AM), represents a big step forward in wound dressings and tissue engineering. Over the past 20 years, 3DP has advanced significantly and is fast growing. This is due to one of the key features of 3DP, the ability to simple customization [25]. With 3DP personalized pharmaceutical forms with flexible dosages, different shapes, multiple active pharmaceutical ingredients (APIs), and modulated release kinetics can be designed [26]. Precision medicine (PM) is a cutting-edge method to handle personalized care that gives a person the proper therapy at the right moment [27]. Furthermore, 3DP is sustainable from an environmentally friendly point of view [28]; chemicals are not always necessary, it uses less energy and produces less material waste. Furthermore, the potential use of different materials helps to choose the most suitable one according to the desired final product and technique employed. Recently, the most advanced application of AM technology has been the production of biocomponents for humans [29]. Various pharmacological investigations and tissue engineering have employed 3D Bioprinting; among which wound dressings have gained popular interest. The constructed scaffold should support specific requirements, such as promoting cell migration, proliferation, and differentiation, removing waste components, and ultimately promoting neovascularization, to support tissue repair [30]. Thanks to an easy fine-tuning of physical and chemical properties, hydrogels have become very popular inks for 3D bioprinting of tissue substitutes, consisting in three-dimensional (3D), hydrophilic, cross-linked polymeric networks that can absorb and store a significant amount of water or biological fluids without losing their structural integrity [31]. Their features make them an ideal choice for wound dressings, especially for their ability to manage exudates and provide a proper moist environment during healing.

Bioinks used to fabricate scaffolds must meet certain criteria to be considered suitable for printing and clinical application [32]. Firstly, bioactivity, biocompatibility, and biodegradability, must be assessed to ensure that cells can adhere to the scaffold to promote new tissue proliferation. Secondly, there must be suitable mechanical properties to give enough support, and finally good printability.

A particular technique in the 3D bioprinting field is coaxial extrusion which generally consists of two flow streams simultaneously extruded in a concentric manner [33]. This is achieved thanks to the nozzle, presenting an outer and an inner section that forms the shell and the core of the extruded filament respectively. Typically, the two materials in the shell and in the core of the nozzle have distinct viscosities; therefore, different extrusion rates are involved. Experimental evaluation is used to determine these flow rates that affect the resulting filament dimensions [34]. The main benefit of this technique is raising the number of printable bioinks thanks to the possibility of combining not only two different hydrogels but also a hydrogel and its suitable cross-linking agent allowing the crosslinking reaction to occur during extrusion, thus promoting better printing resolution. Coaxial bioprinting is particularly used in tissue engineering since it combines different hydrogels and thereby integrates the properties of both materials into the final scaffold.

In this proof-of-concept study, the possibility of combining two novel and appealing manufacturing technologies MFs and 3D bioprinting into

wound dressings was verified for the first time, to the knowledge of the authors. MF was used to produce DPPC:DPPC-PEG:Chol LPs encapsulating TO for a sustained and controlled release on the skin tissues. To the knowledge of the authors, this technique has never been used to produce this type of nanocarriers with TO and it is theorized that MFs will improve particle size control and encapsulation efficiency (EE) as compared to other methods of liposomal synthesis. Coaxial 3D Bioprinting was instead selected to combine TO-LPs and HEC with a hybrid hydrogel composed of SA and CNC enriched with free TO obtaining a burst release of the API and a prompt control of the wound bacterial load. The final resulting scaffolds were then characterized and analysed to prove a proper loading of the LPs, the efficient release of the API, and therefore its antibacterial activity against both clinically relevant Gram-negative and Gram-positive bacterial strains.

2. Materials and methods

2.1. Materials

1,2-dipalmitoyl-*sn*-glycero-3-phosphocholine (>99 %) (DPPC) and cholesterol were purchased from *TCI* (Tokyo, Japan). 1,2-dipalmitoyl-sn-glycerol-3-phosphoethanolamine-[methoxy(polyethylene glycol)-2000] (ammonium salt) (DPPC-PEG2000) (>99 %), thyme oil (TO), ethanol (≥ 99,8 %), Methanol (≥ 99,9 %), acetonitrile (for HPLC, gradient grade, ≥ 99,9 %), trifluoroacetic acid (for HPLC, gradient grade, 99 %) and phosphate-buffered saline tablets (PBS, pH 7.4) were purchased from *Sigma-Aldrich* (Germany). Sodium alginate (SA), hydroxyethyl-cellulose (HEC), $CaCl_2$ 0.1 M solution, trypan blue and nile red were all purchased from *Sigma-Aldrich* (Germany). Cellulose nanocrystals (CNC) were purchased from, the *University of Maine,* USA. Mueller-Hinton Broth was procured from *Oxoid Ltd*, Basingstoke, UK. Chemical structures are shown in (Figs. 1 and 2).

2.2. Liposomes

2.2.1. Preparation of liposomes

PEGylated liposomes were manufactured employing the *Fluigent* MFCS™-EZ (Paris, France) MFs system consisting of two pressure chambers, two flow sensor units (XL, 0–5 mL/min), and a system controller. The chip used is made of *PlasCLEAR* resin from ASIGA and developed using a 3D printing (3DP) technology; method discussed on [35]. The MFs parameters followed in this study have been fine-tuned based on previous works [19,36,37]. A 2:1 ratio between lipids and cholesterol [36], a FRR of 1:3 (1 mL/min:3 mL/min, ethanol:water), thus a TFR of 4 mL/min [19] were used. Phospholipids (DPPC and DPPC-PEG) and cholesterol were dissolved in ethanol (≥ 99,8 % *v*/v) with a 2:2:1 ratio respectively, and kept at a 1 mg/mL concentration [19]. To guarantee full dissolution, the lipid solution was sonicated for 1 min and then, 2 % v/v of TO [37] was added and finally placed in one of the two pressure chambers. For empty liposomal synthesis, TO was omitted from the formulation. The aqueous phase consisted of a PBS solution (pH 7.4).

2.2.2. Dynamic light scattering (Dls) and Z-potential

Liposomes were characterized by determining the average particle size, polydispersity index (PDI), and zeta (ζ) potential. The analysis was conducted using the DLS Nanobrook Omni™ particle sizer (*Brookhaven Instruments*, Holtsville, NY, USA), and each measurement was carried out in triplicate at 25 °C. 20 μL of the samples were 1:100 diluted with 2 mL of PBS (pH 7.4) and put into BI-SCP plastic cuvettes. Both empty LPs and TO-LPs were analysed.

2.2.3. Stability studies

Stability tests were performed on the LP solutions once a week for up to four weeks. The samples were split into three batches and stored at room temperature (RT) and 5 °C, to mimic storage conditions and at 37 °C to mimic body conditions after administration. Each week, the particles' diameter, PDI, and ζ potential were assessed by DLS.

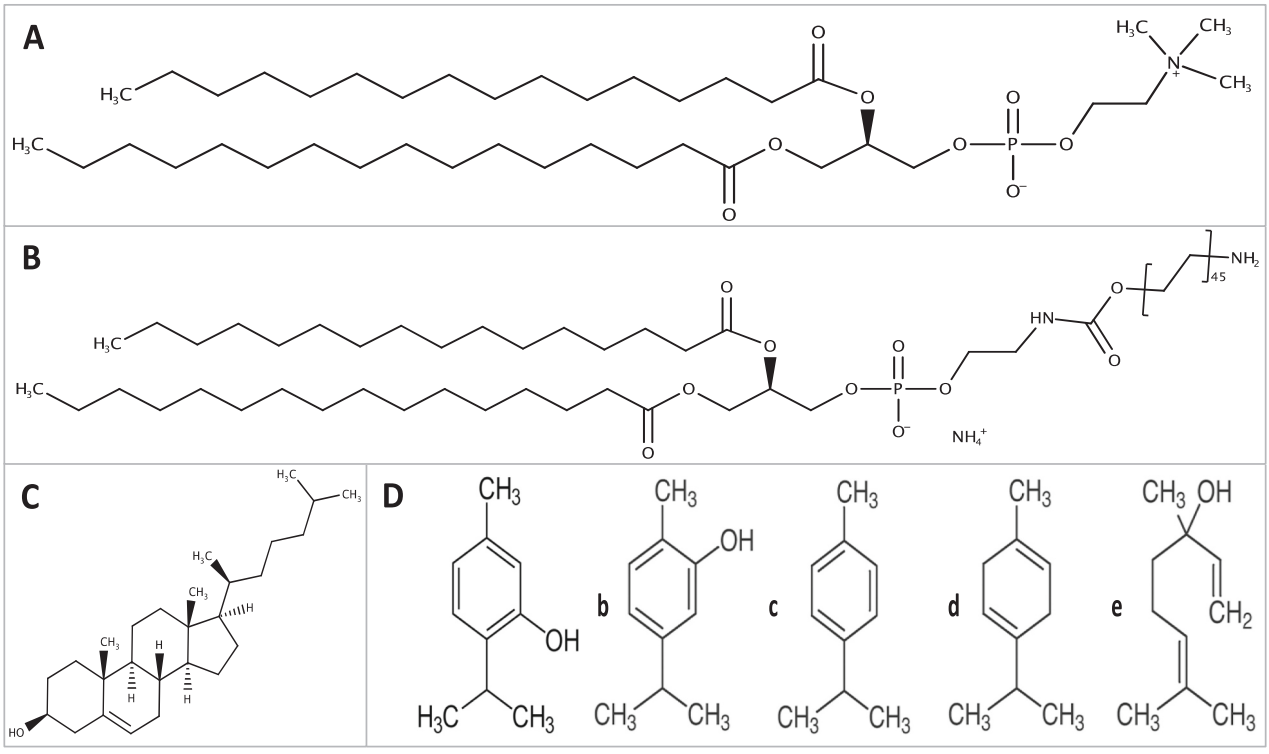

Fig. 1. Chemical structures of A) DPPC-PEG2000; B) DPPC; C) Cholesterol; D) Thyme Oil (TO) components (a. Thymol b. Carvacrol c. p-Cymene d. γ-Terpinene e. Linalool).

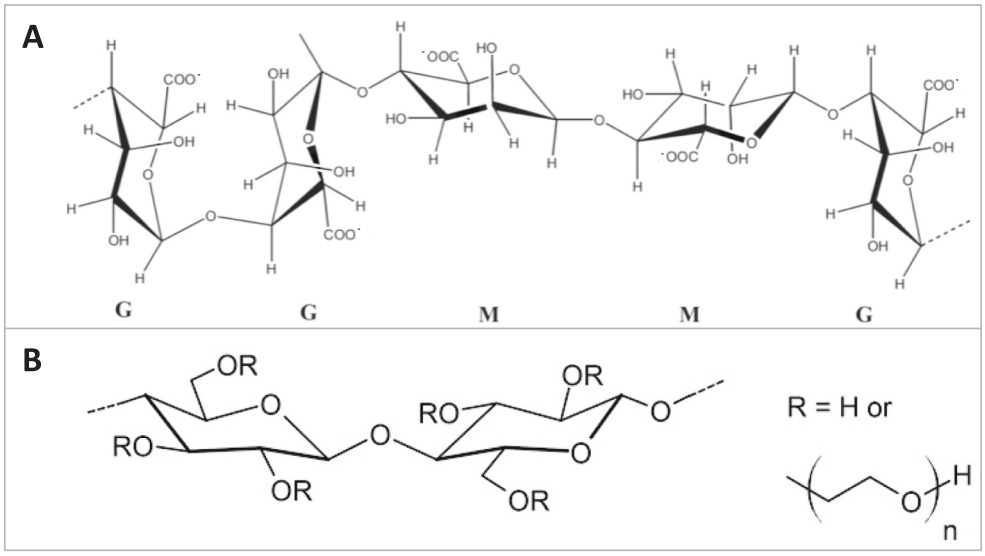

Fig. 2. Chemical structures of A) sodium alginate (SA); B) hydroxyethyl-cellulose (HEC).

2.2.4. Encapsulation efficiency (Ee)

The dialysis method was used to study the EE of the drug into the LPs. Before analysing the samples, dialysis tubes (cellulose membrane, avg. flat width 10 mm, 0.4 in, MWCO 14.000, from *Sigma Aldrich*, Germany) were hydrated and sterilized using boiling water. Then, 1 mL of the LP solution was loaded into the tubes and soaked in 6 mL of methanol. After 30 min, 500 μL of the outer liquid was collected and placed in vials suitable for high-performance liquid chromatography (HPLC). Analysis was carried out in triplicate and referred to a blank. Ultraviolet (UV) High-Performance Liquid Chromatography (UV-HPLC, 1220 Infinity LC™, from *Agilent Technologies,* CA, USA) was used to evaluate the unencapsulated TO in each sample at 293 nm using a C18 column (250 mm × 4.6 mm, from *Thermo Scientific*, MA, USA). The method used for the analysis was modified and adapted from that which was described by Sarfaraz et al. [38]. Each sample underwent a 39.5-min elution gradient consisting of two solvents: (A) 0.05 % *v*/v trifluoroacetic acid (TFA) in water, and (B) 0.05 % v/v TFA in acetonitrile. A 90:10 ratio between solvent A and B was employed from minutes 0 to 20, then 74:26 from min 20 to 35, 35:65 from min 35 to 36, and 90:10 from 36 until 37.5 min. The overall flow rate used was 1.6 mL/min with a sample injection volume of 50 μL. Results were related to a calibration curve obtained for TO by using various concentrations of TO in in methanol working standard solutions and evaluating the resulting peaks. Eq. (1) was used to calculate encapsulation efficiency.

$$\%EE = [(\%\text{of TO added} - \%\text{of unecapsulated TO})/(\%\text{of TO added})]*100 \quad (1)$$

2.2.5. In vitro release

The cumulative in vitro TO release from the LPs was assessed using dialysis bags, as described in Section 2.2.4. After 30 min, the liquid was removed and replaced with fresh methanol (time 0). At 1 h starting from time 0, 500 μL of the outer liquid was taken and placed in HPLC vials for further analysis. The same process was performed also after 2, 4, 6, 24, 48, 72, 168, 240, and 336 h. After every 500 μL withdrawal, the same volume was replaced with fresh methanol that was kept alongside the samples at 37 °C for the entire duration of the analysis to mimic body temperature. Analysis was carried out in triplicate and referred to a blank. The liquid collected was then analysed at the UV-HPLC (1220 Infinity LC™, from *Agilent Technologies,* CA, USA) to evaluate the amount of TO released.

2.3. Hydrogels

2.3.1. Hydrogels preparation

A variety of formulations and combinations of hydrogels were prepared and tested to obtain the most suitable printability and shape fidelity for coaxial 3D bioprinting. Following Pinto et al., previous studies [39], various percentages (%) of SA and CNC (used to improve SA mechanical strength and shear thinning behaviour; therefore its printability) were combined and dissolved in deionized (DI) water: a) 10 % *w/v* of CNC and 2 % w/v of SA; b) 8 % w/v of CNC and 2 % w/v of SA; c) 8 % *w/v* of CNC and 4 % w/v of SA. All the hydrogels were finally enriched with an 8 % *v*/v concentration of free TO, based upon the minimum inhibitory concentration (MIC) and minimum bactericidal concentration (MBC) values found for *S. aureus* and *P.aeruginosa*; described in Section 3.2.3. The TO-LPs solution was made viscous, thus more suitable for 3DP, using 2 % and 3 % w/v of HEC; (Trypan Blue was used as a dye to assess the coaxial printing process). Before increasing the viscosity of the LP solution, dialysis bags (cellulose membrane, avg. flat width 10 mm, 0.4 in, MWCO 14,000, from *Sigma Aldrich*, Germany), hydrated and sterilized, were used to remove any unencapsulated TO. All the hydrogels were left for two nights for curing.

2.3.2. Bioprinting printing parameters

A grid-shaped 20 × 20 × 1.8 mm design was printed through the coaxial technique using an Allevi 2™ 3D bioprinter (*3D Systems*, CA, USA) with a 22 (18 O.D.) cylindrical coaxial nozzle. The selected computer-aided design (CAD) consisted of 6 layers each of which is 0.3 mm high (Fig. 3). In general grid conformations often have higher degrees of structural integrity and grid shapes are a natural choice when it comes to the bioprinting technique as it is better suited to printing at linear orientations. For this investigation, a grid made it simple to adjust the infill parameters so that drug release characteristics could be changed as needed or the DDS could be cut equally, if necessary. Printing parameters have been fine-tuned to obtain the best visual printability; 22 PSI and 77 PSI were chosen as the optimal pressure values for the hydrogel in the filament's core and shell, respectively: (1 PSI = 6.894 kPa). The inner core of the filament embodies TO-LPs and HEC, while the outer shell is represented by a hybrid alginate/CNC hydrogel. After printing, the scaffolds were soaked for 20 min in a $CaCl_2$ solution to let the cross-linking reaction occur and any $CaCl_2$ in excess was removed. Finally, scaffolds were left overnight at room temperature to dry.

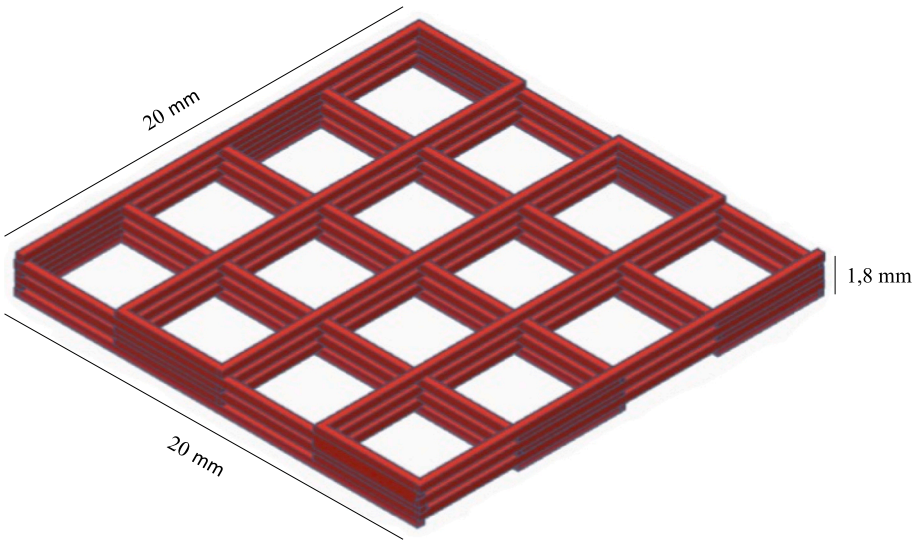

Fig. 3. CAD model of the scaffold.

2.3.3. Physicochemical characterization of the scaffolds

2.3.3.1. Fourier transform infrared spectroscopy (FTIR). Chemical structures of SA, CNC, HEC, TO, and of the final dry scaffolds were analysed using a Nicolet™, iS50 FTIR-ATR spectrometer (*Thermo Scientific*, MA, USA). Absorbance (%) was evaluated in the wavelength range of 4000–600 cm^{-1}. The samples underwent 64 scans with a resolution of 4 cm^{-1} and an interval of 1 cm^{-1}. Background absorption was subtracted from the analysis. The homogeneous distribution of the API in the dry scaffold was also assessed at the FTIR by collecting spectra at the corners and at the middle region of the sample and then compared to verify a similar intensity of the peaks.

2.3.3.2. Confocal microscopy. The LPs' distribution into the filament's inner core was assessed by Confocal Microscope (Stellaris 5™, from *Leica Microsystems*, Germany), equipped with a 20× objective. LPs were previously stained with Nile Red (*Sigma-Aldrich*, Germany) to be suitable for the analysis.

2.3.3.3. Swelling ratio and water content. The scaffold's swelling capability and water content were evaluated over time. The dried scaffold was weighed (m_i) and then placed into 5 mL of PBS (pH 7.4) at 37 °C. At different time points (e.g., 1, 2, 4, 6, 24, and 48 h), the scaffold was taken out from the medium, excess PBS was gently removed, and then reweighed (m_s). Analysis was carried out in triplicate. To calculate the swelling ratio and the scaffold's water content the Eqs. (2) and (3) were used.

$$\mathrm{SWR}\ (\%) = [\mathrm{m(s)} - \mathrm{m(i)}]/\mathrm{m(i)}*100 \tag{2}$$

$$\mathrm{WC}\ (\%) = [\mathrm{m(s)} - \mathrm{m(i)}]/\mathrm{m(s)}*100 \tag{3}$$

Mass loss was instead used to assess the degradation rate. The dry scaffolds were weighed (m_i) and then placed into 5 mL of PBS (pH 7.4) at 37 °C. At each time point (e.g., 24, 48, and 72 h), the scaffold was removed from the medium and let dry overnight for approximately 16 h, and reweighed (m_d). The percentage of mass loss was calculated using Eq. (4).

$$\mathrm{ML}\ (\%) = [\mathrm{m(i)} - \mathrm{m(d)}]/\mathrm{m(i)}*100 \tag{4}$$

All tests were carried out in triplicate.

2.3.3.4. Mechanical studies. Compression tests were performed on the cross-linked scaffolds with a MultiTest 2.5-dV™ from *Mecmesin* (West Sussex, UK) equipped with a 500 N load cell. Tests were conducted at a constant rate of 5 mm/min at room temperature and a total of five samples were tested. Data was collected as Force vs Displacement and then plotted as stress and strain. The Young's Modulus (YM) was determined from engineering stress/strain curves and evaluating the slope of the linear region's trend line.

2.3.4. Drug loading

To verify the amount of TO loaded into the scaffold, the final cross-linked product was placed into 10 mL of PBS (pH 7.4) at room temperature and under mild stirring. After the scaffold was destroyed, all the medium was placed into dialysis bags (cellulose membrane, avg. flat width 10 mm, 0.4 in, MWCO 14.000, from *Sigma Aldrich*, Germany) and soaked in 40 mL of methanol. A 500 μL sample was collected and analysed at the UV-HPLC (1220 Infinity LC™, from *Agilent Technologies,* CA, USA) as described in Section 2.2.4.

2.3.5. In vitro release

The amount of free TO released from the filament's outer shell and the amount of the encapsulated TO released from the filament's inner core; therefore, the overall amount of TO released from the scaffold were assessed. The cross-linked scaffold was put into dialysis bags with 10 mL of PBS and soaked in 40 mL of methanol at 37 °C. At 1, 2, 4, 6, 24, 48, 72, 168, and 240 h time points, a 500 μL sample was collected and placed into vials suitable for UV-HPLC analysis as described in Section 2.2.4. After each withdrawal, the same volume amount was replaced with fresh PBS kept at 37 °C. The PBS used for the in vitro release is simulative of healthy skin tissue.

Cumulative release was calculated, and analysis was carried out in triplicate and referred to a blank.

2.3.6. In vitro antibacterial activity

2.3.6.1. Evaluation of minimum inhibitory concentration (Mic) AND minimum bactericidal concentration (Mbc). The MIC and MBC were determined for TO using the broth microdilution test [40]. Gram-positive, *S. aureus* (ATCC 29213), and Gram-negative, *P. aeruginosa* (PA01) were selected as clinically relevant bacteria. A stock solution of 160 μL/mL TO was prepared in MHB with 10 % *v*/v DMSO [41] and serial two-fold dilutions were performed into 96-well plates. The inoculum to be tested (100 μL, 2×10^6 CFU/mL) was added to each well of the microdilution trays that were incubated for 24 h at 37 °C. Positive

and negative growth controls were included in every assay. MIC was taken as the lowest concentration, producing no visible growth after 24 h. MBC was instead determined by spreading 20 μL of suspension from wells exhibiting no growth onto MHA plates that were incubated for 24 h at 37 °C and examined for 99.9 % killing.

2.3.6.2. Zone of inhibition test. The scaffold's antibacterial activity was measured by the disc diffusion test, through the evaluation of the zone of inhibition [42]. Gram-positive (*S. aureus*), and Gram-negative (*P. aeruginosa*) were selected as the target. Bacteria were cultivated in Mueller-Hinton Broth (MHB, from *Oxoid Ltd*, Basingstoke, UK) at 37 °C and 100 rpm. Approximately 30 mL of the overnight broth cultures were centrifuged at 3000 rpm for 12 min and then the bacterial pellet was re-suspended in PBS (pH 7.4), obtaining an inoculum concentration of 1×10^8 CFU/mL. Sterile cotton swabs were used to inoculate Mueller-Hinton agar plates (MHA, from *Oxoid Ltd*, Basingstoke, UK). Then, the cross-linked scaffolds were placed on the surface of the inoculated MHA plates and incubated at 37 °C for 24 h. A total of 5 samples were analysed and compared to blank scaffolds not containing the API which were used as controls. After 24 h the width of the zones of inhibitions was assessed and compared to the controls. The test was carried out for a total of 48 h.

2.4. Statistical analysis

Experiments were conducted on several samples (n) bigger or equal to three ($n \geq 3$). All data, where possible, are expressed as mean ± standard deviation. One-way ANOVA analysis was used to determine significance using Prism 9 software, with $p \leq 0.05$ used to determine significance.

3. Results and discussion

3.1. Liposomes

3.1.1. Physicochemical analysis

Analysis carried out using DLS, confirmed the repeatability of the method showing an optimal size of 153.06 ± 5.17 nm for the empty DPPC:DPPC-PEG:Chol LPs and 270.08 ± 10.09 nm for the encapsulated LPs. The particles' diameter increase is evidently due to the encapsulation of TO in the lipidic bilayer, owing to its hydrophobic nature. PDI, instead, displays a very slight difference between empty and loaded LPs with a value (<0.30) of 0.19 ± 0.02 and 0.24 ± 0.02 respectively, suggesting a homogeneous dispersion. Alongside controlled NPs' diameter, another key advantage of MFs is the management of the systems' polydispersity. ζ-potential, indicating the system's stability and potential pharmacological interaction, showed values from −7.26 ± 1.34 mV for the blank LPs to −3.23 ± 2.65 mV for the TO-LPs. As expected, all LPs showed a slight anionic charge due to the presence of DPPC [19] and DPPC-PEG. After the TO's encapsulation, a small decrease in the net ζ-potential value was seen and might be addressed to an alteration of the electrokinetic nature of the phospholipids after the API is encapsulated [19]. Meaning that the TO might cause a slightly different orientation of the phospholipids inside the bilayer [43].

3.1.2. Stability studies

Empty LPs were analysed to verify their physical stability as carriers (Fig. 4A) and results were compared to those obtained for the loaded LPs (Fig. 4B). During this period, TO-LPs kept at room temperature and 37 °C showed the best stability, while those kept at 5 °C turned out to be less stable. The same trend was observed for the empty LPs. Flocculation and aggregation phenomena were observed in all three batches kept at different conditions, especially during the third and fourth weeks, indicating that the unmodified system does not have viable stability over

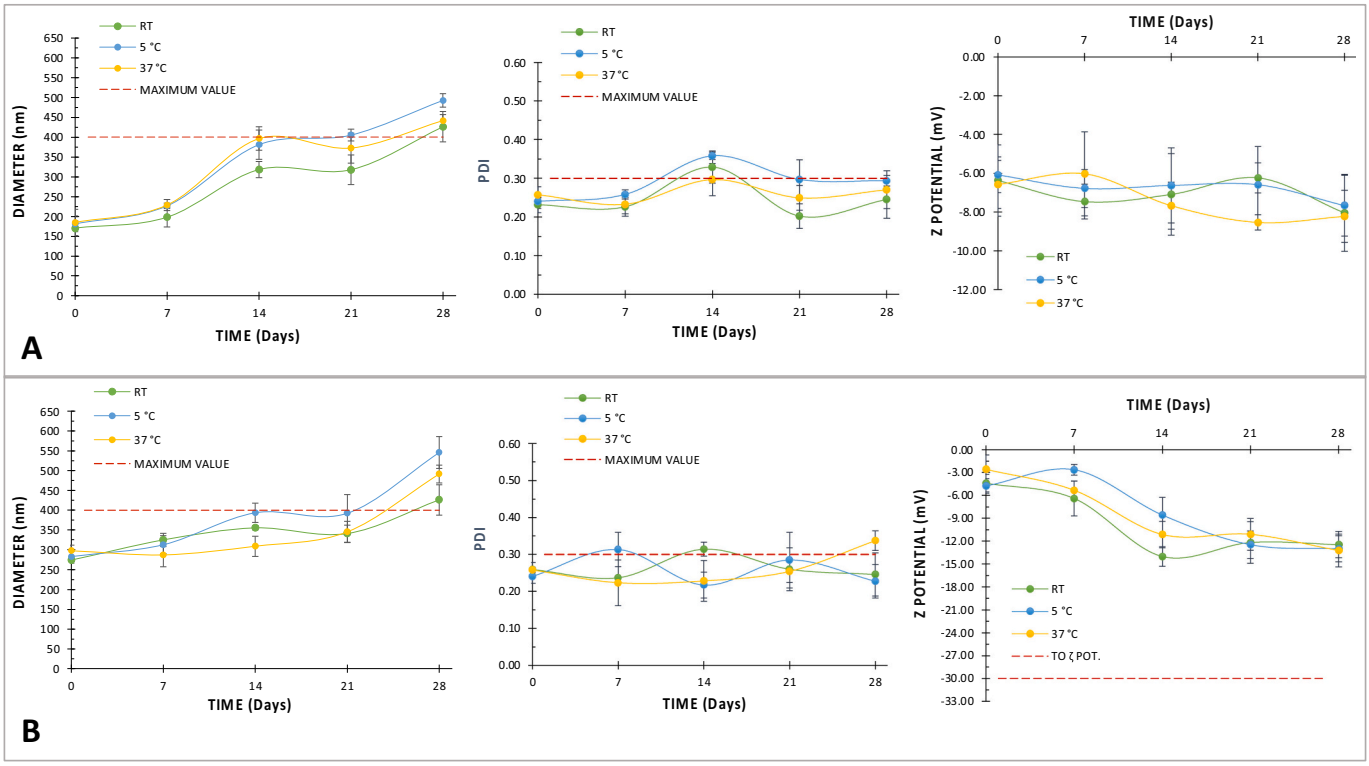

Fig. 4. Stability trend lines at varying storage temperatures of A) empty LPs; B) TO-LPs. For diameter graphs, the line indicated at $n = 400$ nm represents maximum viable particle size for this experimental application. For Polydispersity graphs, the line indicated at $n = 0.3$ represents maximum viable polydispersity for this experimental application.

time. Nevertheless, this does not affect the optimal carrier features of the liposomes as most of the loaded API is released within 10 days and would likely be mostly eliminated in vivo by this stage. During this period LPs still have desirable qualities to deliver TO through the skin-damaged tissues. Particle size is an important feature when considering a topical application as the vesicles must have the proper characteristics to be able to pass through the skin layers to deliver the API. Although, when considering wounds and ulcers, it is also important to consider that the skin tissues are damaged, therefore the physical barrier is interrupted. Because of these aspects and based on previous works [44,45], the maximum acceptable particle size was fixed to be 400 nm. A good homogeneity of the liposomal solution was confirmed by the fact that PDI showed to be generally constant, around 0.25–0.30, throughout the trials with small fluctuations in the values. During the four week-study, ζ-potential showed an increase in the negative value compared to the one observed at time 0, once again this might be due to the API being released from the LPs into the medium, as the droplets of TO itself showed a ζ-potential of -30.00 ± 6.17 mV, this is also confirmed comparing the ζ-potential trend lines of the loaded LPs and the empty ones, where this increase in the anionic charge is not visible.

3.1.3. Encapsulation efficiency and drug release

The MFs manufacturing method has proven itself to be very efficient allowing the encapsulation of high percentages of the starting amount of API; a good advantage when related to other standard procedures [21], especially when considering it to be a sustainable procedure. Relating to the calibration curve, the percentage of TO encapsulated in the LPs was found to be 79.26 ± 0.90 % of the initial quantity added to the lipid phase (Fig. 5A), double the result obtained and previously reported by Cui et al. [21].

Once the quantity of TO carried by the NPs was known, cumulative drug release was assessed and showed a burst release in the amount of API discharged from the liposomes for the first 5 h, up to 28.06 % (Fig. 5B). This burst release profile is due to the steep diffusion gradient caused by a large difference in the TO concentration between the LPs' inner and outer environment, causing the API to release more quickly in the first few hours from the nanocarriers. It has been reported that for a wide range of formulations, the mechanism(s) of release may differ depending on the nanocarrier and release medium [46]. As it is crucial to deliver a bulk dose initially, burst release might have a favourable effect on the antibacterial activity of wound dressings as it helps lower the bacterial load of the wound. The amount of TO in the medium then was observed to have a slower increase in time reaching a release of 47.19 % of the encapsulated quantity within 72 h. After 14 days, the maximum quantity of released TO showed to be 96.50 %. The release can be considered overall satisfying as it is constant and continuous in time, a good feature when it comes to wound healing, helping reduce inflammation, and thus encouraging the tissue repair processes.

3.2. Hydrogels

Sodium alginate (SA), is an appealing material for bioprinting due to its structural resemblance to natural ECM, good biocompatibility, viscosity, and simplicity of room-temperature gelation [47] that may vary in terms of the amounts of β-D-mannuronic acid (M-blocks) and α-L-guluronic acid (G-blocks) and the size of each block according to the derivation source. Gelation occurs in different ways: ionic or covalent cross-linking. Hydrogels made from SA, hence the resulting 3D scaffolds, show good mechanical features and biocompatibility. However, additional biomaterials like cellulose nanocrystals (CNC), gelatin, laponite, or polycaprolactone (PCL) are frequently combined with SA to create a hybrid hydrogel to produce scaffolds with precise pore size and shape [48]. In this way, it is easier to control and optimize chemical and physical parameters, therefore the printing process. Cellulose, instead, is one of the most common polysaccharides found in nature and has also a variety of desirable properties such as biocompatibility, biodegradability, non-toxicity, and low cost. It is a polysaccharide composed of β-1,4 linked D-glucose monomers forming linear chains. Because cellulose itself is poorly soluble in water, its applications are limited. For this reason, one of the most significant commercially available soluble derivatives is hydroxyethyl cellulose (HEC). HEC hydrogels can be easily chemically or physically cross-linked. Cellulose hydrogels show good swelling, antibacterial, and strong mechanical properties, making them suitable for wound healing applications [49] and tissue engineering [50].

The most optimal hydrogel combination for coaxial 3DP was studied and determined to be CNC/SA in a 10:2 ratio and HEC at 3 % *w/v*, based on best printability and shape fidelity results obtained after several experimental trials (Fig. 6F). As can be observed from (Fig. 6), an HEC concentration of 2 % w/v leads to the formulation of a highly-aqueous and liquid-like hydrogel that tends to collapse and lose the filament-like shape, (Fig. 6A, C, E) while increasing the HEC concentration up to 3 % w/v results in a more viscous and solid-like hydrogel that remains stable in the core of the coaxial extruded fibres (Fig. 6B, D, F). The filament's shell consists of CNC/SA, and the optimum ratio of the two components was observed to be 10:2. The 8:4 ratio resulted in a too-hard hydrogel that needed printing pressures over 100 PSI to obtain a complete scaffold (Fig. 6A, B) while decreasing the amount of alginate to 8:2

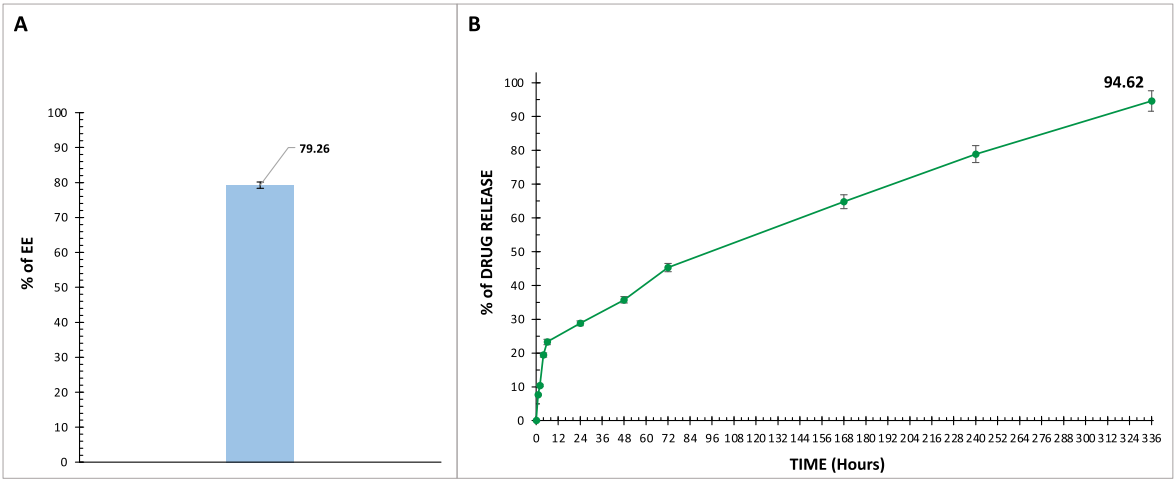

Fig. 5. Data presentation for A) liposomal encapsulation efficiency; B) 14-day Drug Release trend line. All sample data points presented with error bars to show deviation from the mean.

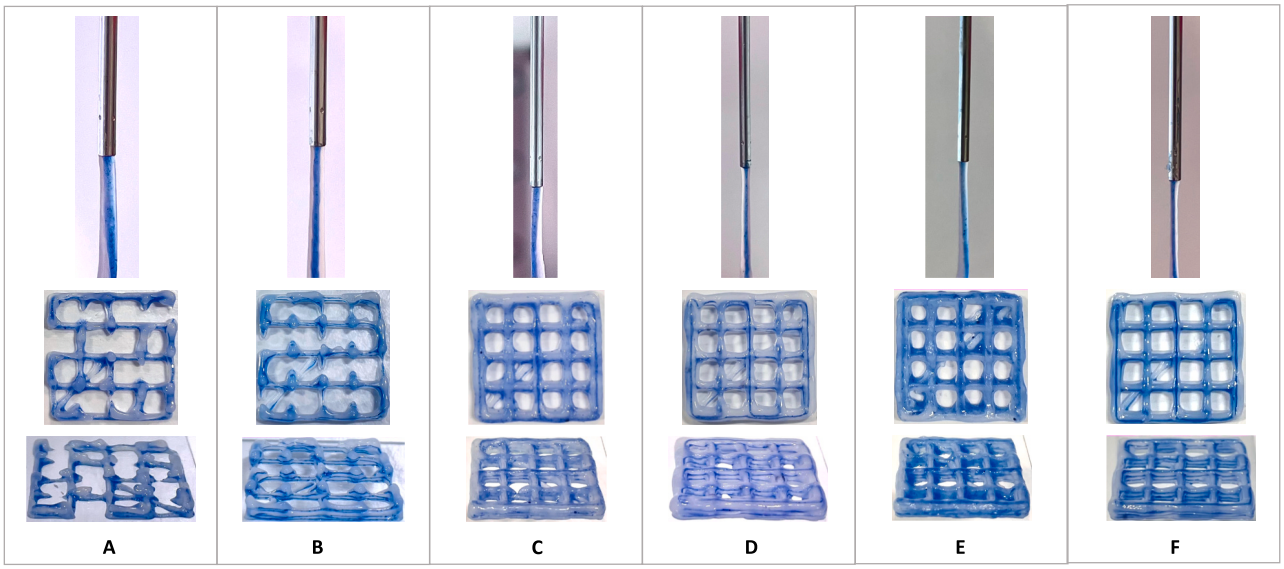

Fig. 6. A) 8:4 (CNC/SA) + 2 % *w/v* HEC; B) 8:4 (CNC/SA) + 3 % w/v HEC; C) 8:2 (CNC/SA) + 2 % w/v HEC; D) 8:2 (CNC/SA) + 3 % w/v HEC; E) 10:2 (CNC/SA) + 2 % w/v HEC; F) 10:2 (CNC/SA) + 3 % w/v HEC.

led to a better formulation and printing resolution (Fig. 6C, D). To obtain an optimal shape fidelity, the percentage of CNC was increased to 10 %, leading to the achievement of the best filament shape and printing resolution (Fig. 6F). Printing parameters were experimentally fine-tuned to obtain the most desirable visual distribution of the two hydrogels and the final scaffold's resolution. The 3DP scaffold's real dimensions resulted to be comparable to the ones selected in the CAD design, with a variability of ±0.50 % of the theoretical values. The scaffold's total volume was instead assessed to be 1.16 ± 0.24 mL.

3.2.1. *Characterization of the scaffold*

3.2.1.1. FTIR. FTIR was used to verify any possible interaction that might have occurred among the materials during the formulation and printing process by comparing SA, CNC, HEC, and the final dry scaffold's spectra (Fig. 7A). For SA, CNC, and HEC a broad band in the range of 3600–3100 cm^{-1} is observed, which refers to the stretching vibration of the O—H groups, weakened by intermolecular hydrogen bonds that occur among the polymer's chains. A medium/weak peak attributed to the symmetric and asymmetric stretching vibration of C—H aliphatic chains is observed at 2933 cm^{-1} for SA, 2903 cm^{-1} for CNC, and 2879 cm^{-1} for HEC. Intense absorption peaks around 1597 and 1403 cm^{-1} are observable for alginate and are attributed to the carboxylate O-C-O symmetrical and asymmetrical stretching vibrations of the carboxyl groups [51]. For CNC and HEC, at 1637 cm^{-1} and 1642 cm^{-1} respectively, a weak peak associated with the O—H bond vibration is observed because of cellulose water absorption [52,53]. An intense broad absorption band is observable around 1200–900 cm^{-1} that corresponds to the stretching of C – H, C – O – C, C – O, and C—H bonds of the glycosidic ring which is present in all the three polysaccharides [53]. TO spectrum instead shows the typical signals of terpene functional groups in the area around 1500 and 800 cm^{-1} and three more intense peaks at 2960, 2926, and 2873 cm^{-1} due to the asymmetrical and symmetrical C—H stretching of CH_3 groups [54]. The FTIR spectrum of $CaCl_2$ cross-linked dry scaffolds displays similar peaks compared with the ones of the starting materials with slight shifts and weakening due to the engagement of the functional groups into intermolecular interactions during the hydrogel formulation. SA's peaks shown at 1597 and at 1403 cm^{-1} and attributed to the carboxyl groups vibrations are shifted to 1608 and 1428 cm^{-1} respectively, which can be associated with the presence of calcium ions forming egg-box structures among SA and cellulose chains

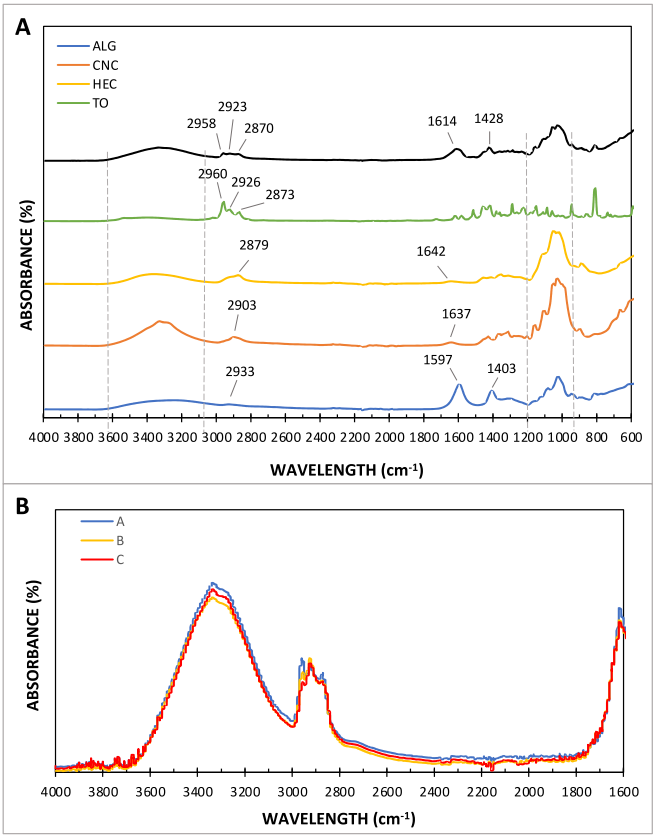

Fig. 7. A) FTIR spectra of SA, CNC, HEC, TO, and of the dry cross-linked scaffold;
B) Homogeneous distribution of free TO in the scaffold assessed by FTIR (A, B and C represent three different random points of the dry scaffold).

[53]. The three peaks attributed to TO's CH_3 vibrations are also observable in the scaffold's spectrum at 2958, 2923, and 2870 cm^{-1}, confirming the presence of TO. The homogeneous distribution of the API in the scaffold was also assessed and is displayed in (Fig. 7B) where three different points of the dry scaffold (A, B, C) were analysed and compared

to each other. The spectra were plotted to show the similarity of the area under the TO's peaks (2960, 2926, and 2873 cm^{-1}), thus its homogeneous distribution into the scaffold.

3.2.1.2. Confocal microscopy. After printing the 3D scaffolds, confocal microscopy was used to verify the actual presence of the TO-LPs in the filament's inner core. As shown in (Fig. 8C) LPs were previously stained with Nile Red (NR). The obtained results (Fig. 8D) indicated that LPs were not affected by the printing process and a homogenous distribution in the filament's core is observable.

3.2.1.3. Swelling ratio and degradation rate. The dry scaffold showed a high swelling capability immediately after 1 h of being soaked in 5 mL of PBS at 37 °C with a maximum peak of 398.20 ± 25.20 % of swelling after 24 h (Fig. 9A). The total water content was assessed to be 78.92 ± 7.30 %. Hydrogels usually carry a water content of around 70–90 % [55], and as expected, this behaviour demonstrates the scaffolds' ability to manage wound exudates while also maintaining a moist environment, conditions that are crucial to promote healing and tissue repair. This property is also particularly useful for immobilizing the hydrophilic outer layer of the LP to the scaffold. After 24 h, a plateau in the swelling trend is observable until a trend reversal occurs due to the degradation process that takes place. This can be confirmed by evaluating the scaffold mass loss through time (Fig. 9B).

3.2.1.4. Mechanical studies. The 3D-printed scaffolds were tested under compression conditions to investigate their mechanical properties, thus their Young Modulus (E), which was calculated as the slope of the linear part of the stress-strain curve and was assessed to be 3.33 ± 0.09 MPa. Under the constant load, the scaffold underwent deformation until a maximum of thinning, highlighting the scaffold's plastic behaviour. Skin is a complex structure, its mechanical properties are often challenging to assess, and its elastic modulus is often variable according to the mechanical test used [56] alongside many other factors such as tissue's age and location. Thus, it's very difficult to compare these studies and define one single value for YM but rather a range of values [56]. The YM of the tested scaffolds can be considered satisfying when compared to the skin's YM that was previously studied and described through indentation tests by Geerligs et al. [57].

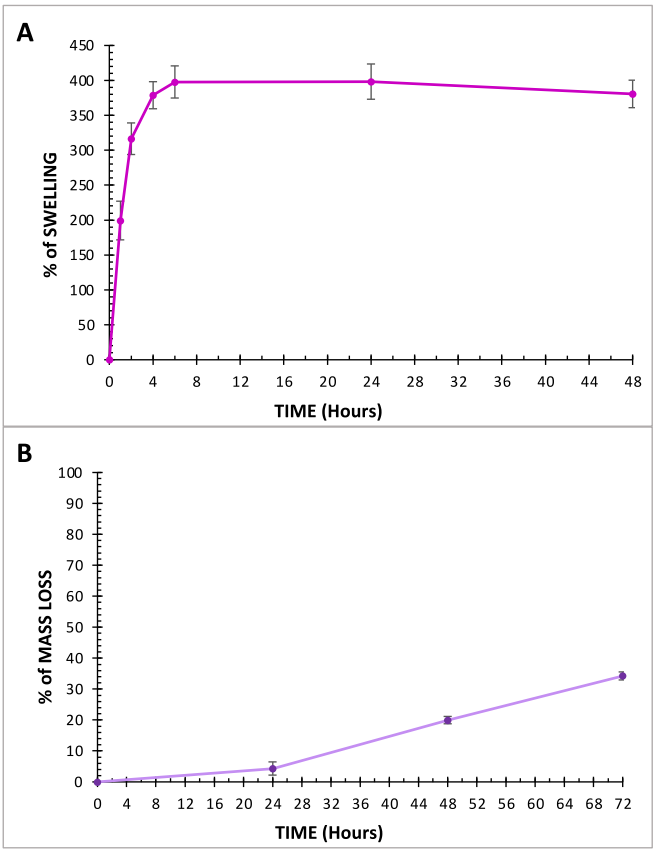

Fig. 9. A) Scaffold's swelling ratio through time; B) Scaffold's mass loss through time.

3.2.2. Drug loading and drug release

The amount of encapsulated TO and free TO loaded in one scaffold were observed to be 5.69 % *v*/v and 16.64 % v/v, respectively. The overall amount of TO loaded in one scaffold was assessed to be 22.32 % v/v. The API release from the core's filament appeared to be very slow in time, and an appreciable release was only seen after 24 h (Fig. 10A). This

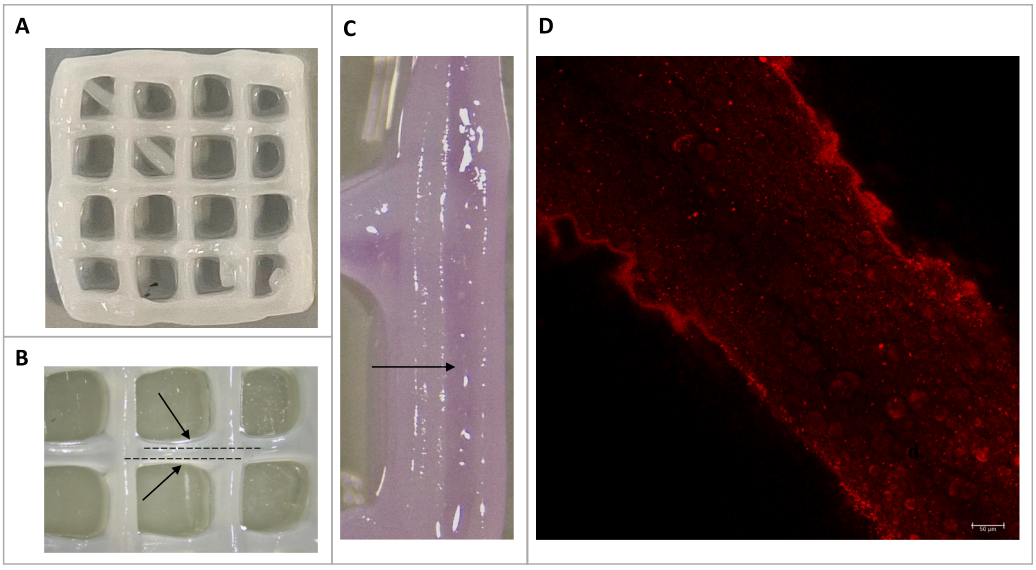

Fig. 8. A) Overview of the 3D-printed scaffold; B) Image of the Coaxial filament under the Leica Microscope; C) Image of the Coaxial filament embedding NR-stained TO-LPs under the Leica Microscope; D) Image of the filament's inner core embedding NR-stained LPs under the Confocal Microscopy Stellaris 5TM, from *Leica Microsystems*. Red Channel: TO-LPs stained with NR embedded in HEC hydrogel (filament's inner core). Black channel: SA/CNC hydrogel (filament's outer shell).

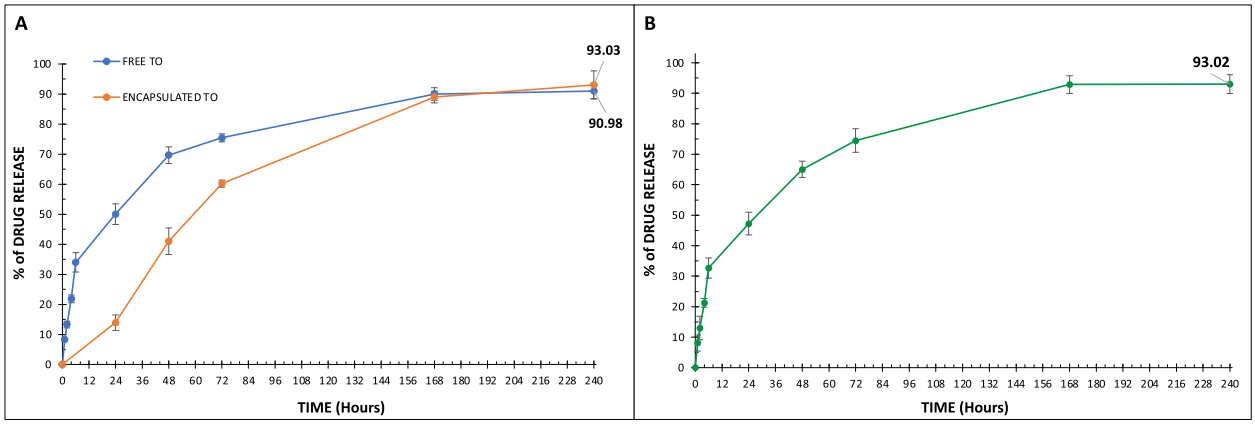

Fig. 10. A) Drug release trend line from the inner core (orange line) and the outer shell (blue line) of the printed filament; B) Cumulative release of the total amount of TO from the 3DP scaffold.

is because TO's diffusion needs time to occur from the LPs' bilayer into the mostly-water-based hydrogel first and towards the outer medium after. For this reason, free TO was also added to the SA/CNC hydrogel, thus to the filament's shell. This provides a bulk release of the essential oil for the first 48 h (Fig. 10B) providing a sterilizing effect on the wound followed by the sustained release of the oil from the LPs that are freed into the skin tissues only during the filament's core degradation. Thanks to the combined release modes and he crossover that occurs around 48 h between the end of the burst and the start of notable LP-driven TO, the risk of AMR following initial burst release (as the concentration gradient diminishes leading to sub-MIC exposure as time progresses) is potentially avoided as the LP-TO release will take over before the potential sub-MIC burst release scenario occurs. Thus, it is possible to say that after the first prompt release of the free API from the shell of the filament which has the greatest bactericidal effect, the LPs in the printed scaffold provide a sustained release of the drug through time, helping to maintain a low bacterial load in the wound environment. The overall release of the API from the 3D printed scaffold is shown in (Fig. 10B) and reaches a maximum of 93.02 ± 3.09 % after 10 days, followed by a stabilization in the release rate.

3.2.3. *In vitro antibacterial studies*

TO's MIC against *S. aureus* (Gram-positive) and *P. aeruginosa* (Gram-negative) was observed to be 0.1 % *v*/v and 0.2 % v/v, while the MBC resulted to be 0.2 % v/v and 1.6 % v/v, respectively. It has been noted in previous studies that the potency of various essential oils has been seen to vary between gram negative and gram-positive bacteria [58,59]. Evaluation of zones of inhibition confirmed the API bulk release in the first 48 h and a good efficacy against the bacterial inoculum. TO release from the scaffold produced an inhibition diameter of 6.18 ± 0.26 cm for *S. aureus* after the first 24 h, and a diameter of 3.33 ± 0.39 cm after 48 h. This significant reduction shows the burst release of free TO that occurs during this time. The diameter of the zone of inhibition in the *P. aeruginosa* resulted to be 2.25 ± 0.26 cm after 24 h with a reduction to no detectable zone of inhibition after 48 h (Fig. 11A and B). After the initial burst release from the LPs, the MIC appeared not to be reachable, which may suggest insufficient clinical effect. However, the intrinsic loading of the TO within the scaffold, coupled with LP release allowed for a sustained bacterial inhibition, especially for *S. aureus.* The differences observed, were expected as the TO's MIC and MBC for *P. aeruginosa* were two- and eight-fold higher compared to the values obtained for *S. aureus*. Thus, the achieved results showed good antibacterial activity of the drug against both bacterial strains, but it must be underlined that Gram-positive bacteria displayed higher sensitivity than the selected Gram-negative bacteria which was more difficult to treat. This can be attributed to differences in the bacterial wall constituents and structure with Gram-negative bacteria, in possessing a more complex cell wall including a second outer membrane, containing lipopolysaccharide, that is not present in Gram-positive bacteria and makes Gram-negative bacteria less vulnerable to a xenobiotic. The loss of efficacy at the 48 h timepoint against *P. aeruginosa* would render these dressings suitable to be changed within this time frame, as continued application beyond this point could lead to further complications of treating the condition. This comes due to the imbalance of efficacy

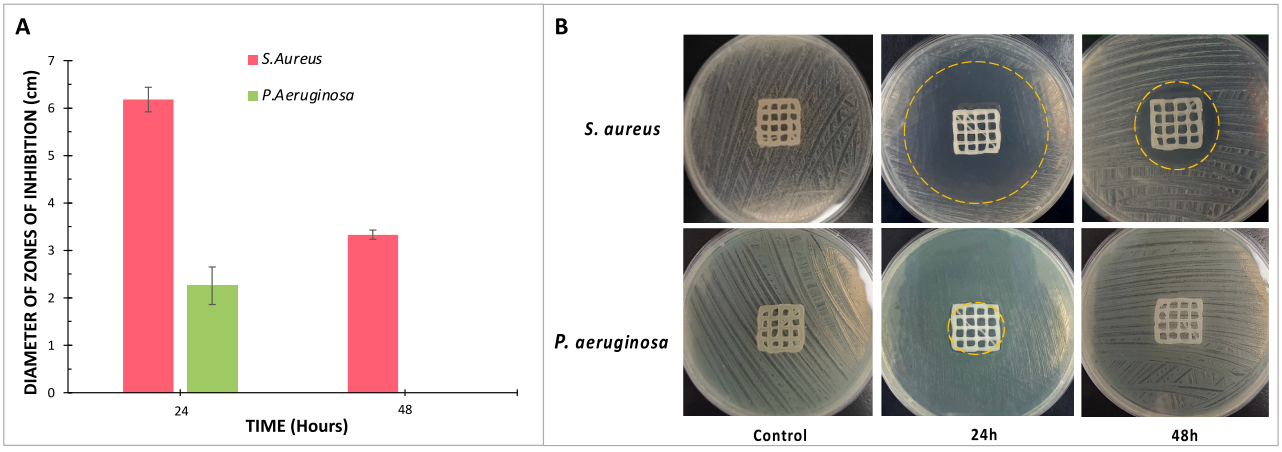

Fig. 11. A) Diameters of the zone of inhibition for *S. aureus* and *P. aeruginosa* after 24 and 48 h; B) Antibacterial activity of the 3DP TO-loaded scaffolds against *S. aureus* and *P. aeruginosa* after 24 and 48 h and compared to the control.

between the gram-positive and gram-negative bacteria, which could lead to "man-made" selection of resistant bacteria if either of the groups is allowed to thrive more within the diabetic environment. Once an ulcer develops, a diabetic patient becomes very vulnerable to infections due to a reduction in innate barrier function. Also, because suffering from a lower efficiency of the immune system, in the presence of hyperglycaemia, phagocytosis and antibacterial capability are considerably decreased [60]. This leads to an additional delay in healing and to an increased potential risk of lower limb amputation.

4. Conclusions

In summary, this novel proof-of-concept study showed how LPs and hydrogels can effectively be combined to create 3DP scaffolds that have both a bulk and sustained release of the loaded API. It can be concluded that MFs and 3D bioprinting can be successfully merged in a versatile manner to manufacture useful carriers that couple various APIs with various hydrogels, thereby obtaining a combination of multiple release ratios. This research opens the gate to the use of different and functionalized liposomal types that can be prepared alongside different scaffold designs. The resulting wound dressings demonstrated an efficacious antibacterial activity that upon further optimisation could prove useful for combating diabetic wound infections This study's primary goal was to demonstrate a synergy between the two methodologies, but further cellular research will be essential to confirm the scaffold's biocompatibility and demonstrate its effectiveness in promoting wound healing. The area of tissue engineering and wound dressing is constantly evolving, and manufacturing these products receives a lot of attention, especially when it comes to chronic wounds that are difficult to treat like DFUs. It is imperative that these treatments are developed and improved to produce efficacious dressings that protect the wound, control the bacterial load, and promote healing processes, as seriously infected wounds continue to be one of the leading causes of hospitalisation and limb amputation, reducing drastically the patient's quality of life.

Sources of funding

This research was not funded.

CRediT authorship contribution statement

Costanza Fratini: Methodology, Investigation, Formal analysis, Writing – original draft, Writing – review & editing. **Edward Weaver:** Methodology, Formal analysis, Conceptualization, Writing – review & editing. **Sofia Moroni:** Methodology, Investigation, Formal analysis, Writing – review & editing. **Robyn Irwin:** Investigation, Writing – review & editing. **Yahya H. Dallal Bashi:** Investigation. **Shahid Uddin:** Writing – review & editing. **Luca Casettari:** Supervision, Writing – review & editing. **Matthew P. Wylie:** Methodology, Writing – review & editing. **Dimitrios A. Lamprou:** Supervision, Conceptualization, Methodology, Writing – review & editing.

Declaration of competing interest

The authors declare that they have no known competing financial interests or personal relationships that could have appeared to influence the work reported in this paper.

Data availability

Data will be made available on request.

Acknowledgements

The authors would like to thank the Marche Region for providing the funding for SM to travel to Queen's University Belfast under the Innovative doctoral programme POR Marche FSE 2014/2020 D.R. 354/2020.

References

[1] E. Everett, N. Mathioudakis, Update on management of diabetic foot ulcers, in: Annals of the New York Academy of Sciences, Blackwell Publishing Inc., 2018, pp. 153–165.
[2] G. Bereda, Complication of diabetes mellitus: microvascular and macrovascular complications, International Journal of Diabetes IJD 3 (1) (2022) 123–128.
[3] Diabetes. 2022; Available from: https://www.who.int/health-topics/diabetes#tab=tab_1.
[4] J.S. Chin, et al., Drug therapies and delivery mechanisms to treat perturbed skin wound healing, Advanced Drug Delivery Reviews. (2019) 2–18. Elsevier B.V.
[5] H. Cho, et al., Acellular and cellular approaches to improve diabetic wound healing, Advanced Drug Delivery Reviews. (2019) 267–288. Elsevier B.V.
[6] K. Glover, et al., 3D bioprinted scaffolds for diabetic wound-healing applications, Drug Delivery and Translational Research 13 (2023) 2096–2109.
[7] A.M. Tatara, D.P. Kontoyiannis, A.G. Mikos, Drug delivery and tissue engineering to promote wound healing in the immunocompromised host: current challenges and future directions, Advanced Drug Delivery Reviews. (2018) 319–329. Elsevier B.V.
[8] J. Al-Shuneigat, et al., Effects of wild Thymus vulgaris essential oil on clinical isolates biofilm-forming bacteria, IOSR Journal of Dental and Medical Sciences 13 (9) (2014) 62–66.
[9] A.P. Perez, et al., The anti MRSA biofilm activity of Thymus vulgaris essential oil in nanovesicles, Phytomedicine 57 (2019) 339–351.
[10] L. Galovičová, et al., Thymus vulgaris essential oil and its biological activity, Plants 10 (9) (2021).
[11] T. Liu, J. Kang, L. Liu, Thymol as a critical component of Thymus vulgaris L. essential oil combats Pseudomonas aeruginosa by intercalating DNA and inactivating biofilm, LWT (2021) 136.
[12] S. Akermi, et al., In-depth study of Thymus vulgaris essential oil: towards understanding the antibacterial target mechanism and toxicological and pharmacological aspects, Biomed. Res. Int. 2022 (2022), 3368883.
[13] L. Risaliti, et al., Liposomes loaded with Salvia triloba and Rosmarinus officinalis essential oils: in vitro assessment of antioxidant, antiinflammatory and antibacterial activities, Journal of Drug Delivery Science and Technology 51 (2019) 493–498.
[14] F.M. Abdelhamed, et al., Antibacterial and anti-inflammatory activities of Thymus vulgaris essential oil Nanoemulsion on acne vulgaris, Microorganisms 10 (9) (2022).
[15] P. Severino, et al., Essential oils as active ingredients of lipid Nanocarriers for chemotherapeutic use, Curr. Pharm. Biotechnol. 16 (4) (2015) 365–370.
[16] G. Ballacchino, et al., Manufacturing of 3d-printed microfluidic devices for the synthesis of drug-loaded liposomal formulations, Int. J. Mol. Sci. 22 (15) (2021).
[17] A. Delama, et al., Microfluidic encapsulation method to produce stable liposomes containing iohexol, Journal of Drug Delivery Science and Technology 54 (2019).
[18] Niculescu, A.G., D.E. Mihaiescu, and A.M. Grumezescu, A review of microfluidic experimental designs for nanoparticle synthesis, in International Journal of Molecular Sciences. 2022, NLM (Medline).
[19] E. Weaver, et al., Microfluidic-mediated self-assembly of phospholipids for the delivery of biologic molecules, Int. J. Pharm. 611 (2022).
[20] T. Terada, et al., Microfluidic preparation of nanoparticles using poly(ethylene glycol)-distearoylphosphatidylethanolamine for solubilizing poorly soluble drugs, J. Pharm. Sci. 111 (6) (2022) 1709–1718.
[21] H. Cui, et al., Effect of nianoliposome-encapsulated thyme oil on growth of Salmonella enteritidis in chicken, Journal of Food Processing and Preservation 41 (6) (2017).
[23] S.N. Park, et al., Preparation of quercetin and rutin-loaded ceramide liposomes and drug-releasing effect in liposome-in-hydrogel complex system, Biochem. Biophys. Res. Commun. 435 (3) (2013) 361–366.
[24] M. Ullrich, et al., Encapsulation stability and temperature-dependent release kinetics from hydrogel-immobilised liposomes, J. Colloid Interface Sci. 394 (2013) 380–385.
[25] S. Moroni, L. Casettari, D.A. Lamprou, 3D and 4D printing in the fight against breast Cancer, Biosensors (Basel) 12 (8) (2022).
[26] M.R.P. Araujo, et al., The digital pharmacies era: how 3D printing technology using fused deposition modeling can become a reality, Pharmaceutics 11 (3) (2019).
[27] K. Jain, et al., 3D printing in development of nanomedicines, Nanomaterials (Basel) 11 (2) (2021).
[28] E. Weaver, C. O'Hagan, D.A. Lamprou, The sustainability of emerging technologies for use in pharmaceutical manufacturing, Expert Opinion on Drug Delivery 19 (7) (2022) 861–872.
[29] C.M. Thakar, et al., 3d printing: basic principles and applications, Materials Today: Proceedings 51 (2022) 842–849.
[30] A. Habib, et al., 3D printability of alginate-Carboxymethyl cellulose hydrogel, Materials (Basel) 11 (3) (2018).
[31] A.A. Sitab, et al., Fabrication of chitosan-based biomaterials: techniques and designs, Engineering Materials for Stem Cell Regeneration. (2021) 455–518.
[32] A. Parak, et al., Functionalizing bioinks for 3D bioprinting applications, Drug Discov. Today 24 (1) (2019) 198–205.
[33] T.S. Mohan, et al., 3D coaxial bioprinting: process mechanisms, bioinks and applications, Prog Biomed Eng (Bristol) 4 (2) (2022).

[34] A. Kjar, et al., Engineering of tissue constructs using coaxial bioprinting, Bioact Mater 6 (2) (2021) 460–471.
[35] F. Sommonte, et al., In-house innovative “diamond shaped” 3D printed microfluidic devices for lysozyme-loaded liposomes, Pharmaceutics 14 (11) (2022).
[36] M.L. Briuglia, et al., Influence of cholesterol on liposome stability and on in vitro drug release, Drug Delivery and Translational Research 5 (3) (2015) 231–242.
[37] S. Jabraeili, et al., Nanoliposomal thyme (Thymus vulgaris) essential oil: effects of formulation parameters, Food Sci. Technol. Int. 28 (3) (2022) 257–272.
[38] D. Sarfaraz, M. Rahimmalek, G. Saeidi, Polyphenolic and molecular variation in Thymus species using HPLC and SRAP analyses, Sci. Rep. 11 (1) (2021) 5019.
[39] E.A. Pinto, J.L. Dávila, M.A. d'Ávila, Rheological studies on nanocrystalline cellulose/alginate suspensions, J. Mol. Liq. 277 (2019) 418–423.
[40] L. Carson, et al., Antibiofilm activities of 1-alkyl-3-methylimidazolium chloride ionic liquids, Green Chemistry 11 (4) (2009).
[41] T. Sripahco, et al., Chemical composition, antioxidant, and antimicrobial activity of Elsholtzia beddomei C. B. Clarke ex Hook. f. essential oil, Sci Rep 12 (1) (2022) 2225.
[42] M.P. Wylie, et al., Phosphonium ionic liquid-infused poly(vinyl chloride) surfaces possessing potent antifouling properties, ACS Omega 5 (14) (2020) 7771–7781.
[43] E. Chibowski, A. Szcześ, Zeta potential and surface charge of DPPC and DOPC liposomes in the presence of PLC enzyme, Adsorption 22 (4–6) (2016) 755–765.
[44] D.D. Verma, et al., Particle size of liposomes influences dermal delivery of substances into skin, Int. J. Pharm. 258 (1–2) (2003) 141–151.
[45] Z. Li, et al., Increased cutaneous wound healing effect of biodegradable liposomes containing madecassoside: preparation optimization, in vitro dermal permeation, and in vivo bioevaluation, Int. J. Nanomedicine 11 (2016) 2995–3007.
[46] Bhattacharjee, S., Understanding the burst release phenomenon: toward designing effective nanoparticulate drug-delivery systems. 23 Dec 2020.
[47] J.K. Carrow, et al., Polymers for bioprinting, in essentials of 3D, Biofabrication and Translation. (2015) 229–248.
[48] Z. Yao, et al., Biomimetic multilayer polycaprolactone/sodium alginate hydrogel scaffolds loaded with melatonin facilitate tendon regeneration, Carbohydr. Polym. 277 (2022), 118865.
[49] R. Kundu, et al., Cellulose hydrogels: green and sustainable soft biomaterials. Current research in green and sustainable, Chemistry (2022) 5.
[50] L.H. Fu, et al., Multifunctional cellulose-based hydrogels for biomedical applications, J. Mater. Chem. B 7 (10) (2019) 1541–1562.
[51] M. Fertah, et al., Extraction and characterization of sodium alginate from Moroccan Laminaria digitata brown seaweed, Arab. J. Chem. 10 (2017) S3707–S3714.
[52] Y. Tang, et al., Preparation and characterization of nanocrystalline cellulose via low-intensity ultrasonic-assisted sulfuric acid hydrolysis, Cellulose 21 (1) (2013) 335–346.
[53] N. Naseri, et al., Nanocellulose-based interpenetrating polymer network (IPN) hydrogels for cartilage applications, Biomacromolecules 17 (11) (2016) 3714–3723.
[54] M. Catauro, et al., Chemical analysis and anti-proliferative activity of Campania Thymus vulgaris essential oil, J. Essent. Oil Res. 29 (6) (2017) 461–470.
[55] O.C. Gunes, A. Ziylan Albayrak, Antibacterial polypeptide nisin containing cotton modified hydrogel composite wound dressings, Polym. Bull. 78 (11) (2020) 6409–6428.
[56] J.C.J. Wei, et al., Allometric scaling of skin thickness, elasticity, viscoelasticity to mass for micro-medical device translation: from mice, rats, rabbits, pigs to humans, Sci. Rep. 7 (1) (2017) 15885.
[57] M. Geerligs, et al., In vitro indentation to determine the mechanical properties of epidermis, J. Biomech. 44 (6) (2011) 1176–1181.
[58] C.A. Semeniuc, C.R. Pop, A.M. Rotar, Antibacterial activity and interactions of plant essential oil combinations against gram-positive and gram-negative bacteria, J. Food Drug Anal. 25 (2) (2017) 403–408.
[59] V.V. Ebani, et al., In vitro antimicrobial activity of Thymus vulgaris, Origanum vulgare, Satureja montana and their mixture against clinical isolates responsible for canine otitis externa, Veterinary Sciences 10 (1) (2023) 30.
[60] A. Alavi, et al., Diabetic foot ulcers: Part I. Pathophysiology and prevention, Journal of the American Academy of Dermatology 70 (1) (2014) 1.e1–1.e18.